

## 3D PRINTING

# Self-enhancing sono-inks enable deep-penetration acoustic volumetric printing

Xiao Kuang<sup>1†</sup>, Qiangzhou Rong<sup>2†</sup>, Saud Belal<sup>2†</sup>, Tri Vu<sup>2</sup>, Alice M. López López<sup>1</sup>, Nanchao Wang<sup>2</sup>, Mehmet Onur Arıcan<sup>1</sup>, Carlos Ezio Garciamendez-Mijares<sup>1</sup>, Maomao Chen<sup>2</sup>, Junjie Yao<sup>2\*</sup>, Yu Shrike Zhang<sup>1\*</sup>

Volumetric printing, an emerging additive manufacturing technique, builds objects with enhanced printing speed and surface quality by forgoing the stepwise ink-renewal step. Existing volumetric printing techniques almost exclusively rely on light energy to trigger photopolymerization in transparent inks, limiting material choices and build sizes. We report a self-enhancing sonicated ink (or sono-ink) design and corresponding focused-ultrasound writing technique for deep-penetration acoustic volumetric printing (DAVP). We used experiments and acoustic modeling to study the frequency and scanning rate-dependent acoustic printing behaviors. DAVP achieves the key features of low acoustic streaming, rapid sonothermal polymerization, and large printing depth, enabling the printing of volumetric hydrogels and nanocomposites with various shapes regardless of their optical properties. DAVP also allows printing at centimeter depths through biological tissues, paving the way toward minimally invasive medicine.

Three-dimensional (3D) printing is attracting increasing attention with its ability to directly fabricate geometrically complex constructs for prototypes (1), high-performance materials (2, 3), multi-material parts (4, 5), flexible electronics (6, 7), medical devices (8), and engineered tissues (9, 10). Various printing modalities, such as extrusion printing, inkjet printing, stereolithography, and powder-bed fusion, have been developed to print different materials, including thermoplastics, liquid photoinks, and solid polymer powders, among others (11, 12). These printing methods use light or photothermal heating as energy sources to trigger selective material solidification in a layer-by-layer fashion. A build platform controlled by a linear translation stage is usually required to support the stepwise material solidification. Emerging printing techniques accompanied by new photocurable inks have been developed to improve printing speed (13, 14), printing resolution (15–17), and printout functionality (18, 19). Volumetric printing that creates 3D constructs without a build platform or an ink-renewal step can substantially improve printing speed and surface quality (20–23). The existing volumetric printing techniques use light to achieve selective photopolymerization in the volumes of optically transparent inks (24–26). However, the light attenuation by inks themselves, the presence of functional additives (e.g., photoabsorbers and fillers), or/and already-cured parts have imposed con-

straints on the material choices and the build sizes for light-based volumetric printing. Although infrared (IR) light can be used to improve light penetration to several millimeters (26–28), it remains technically challenging to deliver light deep into optically scattering media, such as biological tissues. Therefore, light-based volumetric printing has intrinsic limitations for application in deep-penetration digital manufacturing schemes and, further, in minimally invasive fabrication scenarios (29, 30).

Compared with light, ultrasound waves (<10 MHz) can penetrate >100 times deeper into optically scattering materials and thus hold promise for depositing energy to trigger polymerization at depths (31). By means of an ultrasound bath or horn-based reactors, ultrasound waves can generate reactive oxygen species (ROS; i.e., hydroxyl and peroxide radicals) by cavitation of water, enabling vinyl monomer polymerization for hydrogel formation in several to tens of minutes (32, 33). Ultrasound waves can also be focused into a small volume using a focused ultrasound (FUS) transducer. A FUS transducer can generate acoustic waves with positive and negative pressures alternating at megahertz frequency and propagating along the depth direction, and the high acoustic energy can be delivered into the focal zone with high precision. Previously, cavitation-based ultrasound printing was achieved by curing a polydimethylsiloxane resin (34). However, a build platform was required, and only relatively simple geometries could be printed, because the intense acoustic streaming by the high acoustic pressure disturbed the local ink at the focus region.

Here, we report phase-transition viscoelastic sonicated inks (hereafter, sono-inks) that simultaneously allow deep acoustic penetration, low

acoustic streaming, and rapid sonothermally induced radical polymerization, collectively enabling deep-penetration acoustic volumetric printing (DAVP) (Fig. 1A). DAVP takes advantage of rapid material solidification by the sonothermal effect of the FUS focus in a viscoelastic sono-ink, which provides the building voxel to construct 3D objects without the need for a build platform. In DAVP, the FUS waves deliver deep-penetration acoustic energies with pressures up to several tens of megapascals to the local region at a distance of up to 64 mm (focal length) (Fig. 1B). The small oval-shaped FUS focal zone (full width at half maximum of the acoustic pressure field: 0.3 to 0.7 mm) is further narrowed by the nonlinear acoustic propagation effect at high acoustic pressure (35), collectively facilitating fast, high-resolution printing (Fig. 1C and fig. S1). Consequently, DAVP allows us to print geometrically complex materials precisely and volumetrically, even through nontransparent and optically scattering materials.

## DAVP principle and self-enhancing sono-ink design

Traditionally, ultrasound-mediated cross-linking of the vinyl-based hydrogel precursors is slow, because of the low concentration of ROS generated by ultrasound-induced cavitation (see supplementary text in the supplementary materials). Besides, ROS can be rapidly quenched or diluted by robust acoustic streaming. Our simulation results showed that high-viscosity fluids could significantly reduce the acoustic streaming velocity (Fig. 1D and fig. S2). However, highly viscous ink feedstocks usually exhibit high acoustic attenuations and thus substantially reduce acoustic penetration (36). We hypothesized that a meticulously designed multicomponent viscoelastic sono-ink should suppress acoustic streaming while facilitating a fast sonothermal effect and thus trigger rapid and spatial radical polymerization of vinyl precursors for a deep-penetration fabrication scheme.

To formulate such a proof-of-concept sono-ink, we selected a vinyl oligomer of poly(ethylene glycol) diacrylate (PEGDA) as the base component, agar microparticles as the rheology modifier, poly(*N*-isopropyl acrylamide) (PNIPAm) as the self-enhancing acoustic absorber, and ammonium persulfate (APS) as the thermal initiator (fig. S3). Compared with PEGDA ink, PEGDA-based sono-ink (PEGDA/agar/PNIPAm at, for example, 20/10/3 wt/wt/wt % ratio) showed enhanced viscosities owing to the coil-to-globule phase transition of PNIPAm [transition temperature ( $T_i$ ) = 34° to 36°C] (Fig. 1E and fig. S4). The viscosity of the sono-ink increased 92-fold, from 2.0 to 185.3 Pa·s, when heated from 25°C to 40°C at low shearing (0.05 Hz) (fig. S4C). Meanwhile, the sono-ink showed prominent shear

<sup>1</sup>Division of Engineering in Medicine, Department of Medicine, Brigham and Women's Hospital, Harvard Medical School, Cambridge, MA 02139, USA. <sup>2</sup>Department of Biomedical Engineering, Duke University, Durham, NC 27708, USA.

\*Corresponding author. Email: junjie.yao@duke.edu (J.Y.); yszhang@bwh.harvard.edu (Y.S.Z.)

†These authors contributed equally to this work.

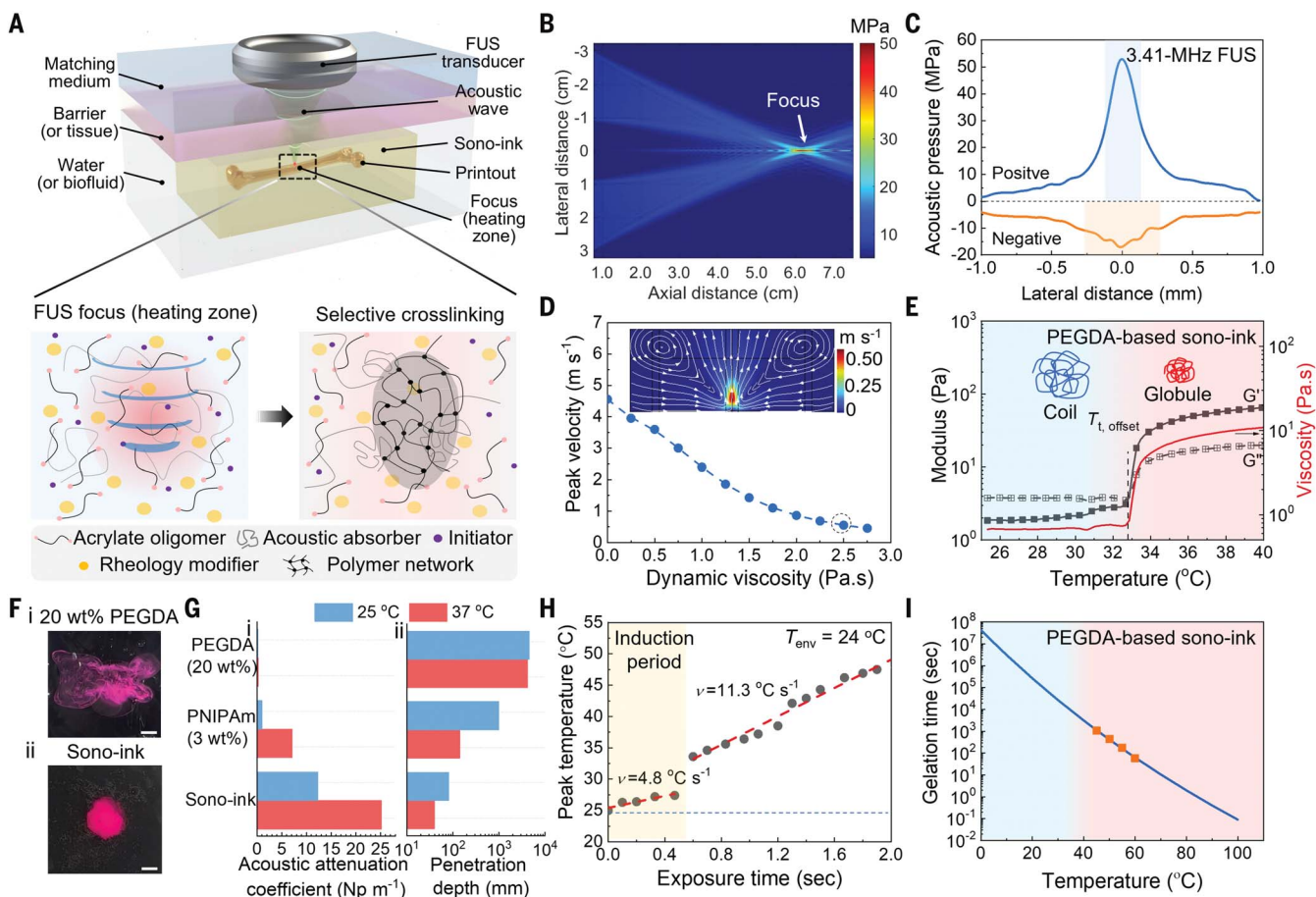


**Fig. 1. Working principle of DAVP and design of self-enhancing sono-ink.**

(A) Scheme showing acoustic printing of constructs by selective curing of sono-ink using deep-penetration FUS. The sonothermal effect enhanced by the phase-transitioning acoustic absorber triggers the decomposition of the initiator for local polymerization of acrylate oligomers into polymer networks at the heating zone. (B) Simulated acoustic pressure field in water for the 3.41-MHz FUS transducer with an acoustic power of 50 W, using the nonlinear acoustic model. (C) Lateral pressure distribution of the 3.41-MHz FUS transducer with an output voltage ( $V_p$ ) of 192 V. The shaded regions show the full width at half maximum of the positive and negative pressures (0.3 to 0.7 mm). (D) Simulated maximum velocity in the focal region versus the dynamic viscosity of the sono-ink. Inset acoustic streaming simulation shows the velocity field of fluids with a viscosity of 2.5 Pa.s.

(E) Oscillation temperature sweep shows the enhanced moduli and viscosity of PEGDA-based sono-ink at a transition temperature (33° to 36°C) due to coil-to-globule transition of PNIPAm. (F) Acoustic streaming in different fluids at the focal region of 3.41-MHz FUS for 2-s exposure: 20 wt % PEGDA (i) and PEGDA/agar/PNIPAm sono-ink (ii). Scale bars: 5 mm. (G) Acoustic properties of the PEGDA/agar/PNIPAm sono-ink and its key components under 3.41-MHz FUS at 25° and 37°C: acoustic attenuation coefficient in linear scale (i) and penetration depth in log scale (ii). (H) Peak temperature in sono-ink at the heating zone near the FUS focus as a function of exposure time, at an environment temperature of 24°C. (I) Gelation time measured by rheology as a function of the curing temperature for PEGDA-based sono-ink supplemented with 1.0 w/w % APS. Orange squares represent the experiment data, and the solid blue line is the fitting curve by the Arrhenius law.

thinning, as reflected by an 87% reduction in viscosity under 100-Hz shearing at 25°C (fig. S4). This sono-ink design concept was generalizable to different formulations, including those using vinyl oligomers from natural polymers [e.g., gelatin methacryloyl (GelMA)] (fig. S4) or different phase-transition polymers with tunable transition temperatures ( $T_{t,offset} = 20.9^\circ$  to  $38.5^\circ$ C) (fig. S5 and table S1), as well as formulations adding various nanoparticles (table S2). Our sono-ink design resolved the long-standing dilemma between acoustic penetration depth and acoustic streaming. On the one hand, the shear thinning facilitated deep acoustic penetration under high-frequency acoustic waves. On the other

hand, the viscosity enhancement by phase transition substantially reduced acoustic streaming. In contrast to the violent streaming in the PEGDA solution, the self-enhancing sono-ink exhibited negligible fluid flow at the FUS focus (Fig. 1F, fig. S6, and movie S1), as supported by the simulation (Fig. 1D).

To investigate the sono-ink's self-enhanced acoustic attenuation effect, we measured the acoustic attenuation coefficient ( $\alpha$ ) of the proof-of-concept sono-ink and key components at various temperatures (fig. S7). Because of the phase transition, the  $\alpha$  of the PNIPAm (3 wt %) aqueous solution and PEGDA-based ink at the ultrasound frequency of 3.41 MHz increased with the temperature, for example, by 600 and

100%, respectively, from 25°C to 37°C (Fig. 1G). The  $\alpha$  of the sono-ink (containing both PEGDA and PNIPAm) was 25.2 nepers per meter ( $\text{Np m}^{-1}$ ) at a temperature of 37°C, which was 86-fold larger than that of 20 wt % PEGDA alone but still much lower than the  $\alpha$  of soft biological tissues under the same conditions (table S3). Despite the self-enhanced acoustic attenuation, the acoustic waves could still achieve a large penetration depth ( $D_p = 1/\alpha$ ) of 40 mm into the sono-ink at 37°C (Fig. 1G).

As a direct result of self-enhanced acoustic attenuation and viscosity, the phase-transition sono-ink exhibited a fast and self-enhanced heating effect. The PNIPAm solution and the sono-ink could be rapidly heated up to between

60° and 80°C at the heating zone after seconds of FUS exposure at mild input powers (<100 W) (fig. S8 and movie S2). PNIPAm played a critical role in achieving fast sonoheating, in contrast to the negligible heating of the 20 wt % PEGDA solution. To further investigate the self-enhanced heating effect, the heating-zone temperatures as a function of FUS exposure time were monitored by an IR thermal camera during FUS exposure at different environmental temperatures ( $T_{\text{env}}$ ). At a  $T_{\text{env}}$  of 24°C—far below the  $T_{\text{t, offset}}$  of PNIPAm—the peak temperature at the heating zone first showed a slow heating rate ( $4.8^\circ\text{C s}^{-1}$ ) and then, after the temperature leap at 36°C, a much-enhanced heating rate ( $11.3^\circ\text{C s}^{-1}$ ), as a result of the phase transition (Fig. 1H). The slow heating period, called the induction period, was reduced from 0.5 s to 0.1 s by raising the  $T_{\text{env}}$  to 33°C (close to  $T_{\text{t, offset}}$ ) and entirely eliminated at  $T_{\text{env}} = 35^\circ\text{C}$  ( $>T_{\text{t, offset}}$ ) (fig. S9 and movie S3). In our printing technique,  $T_{\text{env}}$  was set slightly lower than  $T_{\text{t, offset}}$  to allow for confined sonoheating at the FUS focus. It is worth noting that, as in thermal-based tissue ablation (37), our self-enhancing sono-ink enabled a prominent sonothermal effect under a high-duty cycle of 90%. We did not observe FUS-induced cavitation activities, as validated by active cavitation mapping (fig. S10 and movie S4). Therefore, it was concluded that FUS-induced cavitation is not responsible for the sono-ink solidification.

The self-enhanced sonothermal effect was leveraged to trigger the radical polymerization of vinyl oligomers for fast gelation. The gel-point conversion of the PEGDA-based sono-ink was ~0.3, as measured by Fourier transform infrared spectroscopy (fig. S11). In the presence of APS, the sono-inks proceeded with (sono)thermal-induced gelation, as illustrated by the rheological measurement (fig. S12). The temperature-sensitive gelation time ( $t_{\text{gel}}$ ) followed the Arrhenius law, revealing a high activation energy ( $171 \text{ kJ mol}^{-1}$ ) (eq. S10). Consequently, long shelf life ( $t_{\text{gel}} = 167$  days at 4°C) and on-demand fast curing ( $t_{\text{gel}} = 1.9$  s at 80°C) were simultaneously achieved (Fig. 1I).

### DAVP printing-resolution characterizations

We developed a 3D FUS printer, which was equipped with a FUS transducer at three ultrasound frequencies (2.05, 3.41, and 6.86 MHz), a 3D motorized translation stage, and a printing control system (fig. S13; see materials and methods in the supplementary materials for further details). We first studied the single-point printing resolution of DAVP. Upon FUS exposure in the sono-ink, a whitening region formed and quickly expanded beyond the FUS heating zone (fig. S14 and movie S5), as PNIPAm simultaneously acted as the self-enhancing acoustic absorber and the temperature indi-

cator (38). IR thermal images of the sono-ink surface showed a clear temperature increase forming a heating zone (Fig. 2A). The heated surface area (diameter of up to 4 mm) was larger than the focal zone of the FUS transducer (0.45 mm at 3.41 MHz) because of the rapid thermal diffusion. Upon cooling, a piece of opaque solid formed at the center of the heating zone, and the uncured sono-ink returned to its original color. By comparing the curing size with the heating-zone temperature profile, we found that the curing temperature threshold was  $T_c = 67^\circ\text{C}$  for the PEGDA-based sono-ink supplemented with 0.5 w/w % APS. Because of heat diffusion by the low-power cumulative FUS, the curing size increased with input power (or peak acoustic pressure) and exposure time (Fig. 2B and fig. S15). The nonlinear acoustic effect resulted in elevated acoustic intensity at the FUS focus by increasing the peak pressure and reducing the focal region (39, 40), as shown by our nonlinear acoustic modeling (fig. S16). The simulation also captured the nonlinear acoustic propagation in the sono-ink, exhibiting weak reflection and scattering by different boundaries (such as plastics and tissues) in the far field (fig. S17), and negligible acoustic reflection and scattering at the interface formed by the sono-ink phase transition (fig. S18). Using the numerically modeled temperature map and the measured  $T_c$ , we investigated the increasing single-point curing size (0 to 4 mm in diameter) as a function of peak acoustic pressure (35 to 55 MPa) and exposure time (0 to 5 s) (Fig. 2C, fig. S19, and movie S6).  $T_c$  of the sono-inks could be readily reduced from  $67^\circ\text{C}$  to  $62^\circ\text{C}$  by increasing the APS concentration, because of the enhanced reaction rate (fig. S20 and eq. S8). Additionally, increasing the PEGDA concentration (40 wt %) increased the apparent  $T_c$  of the sono-ink, likely owing to additional heating by the exothermic effect of polymerization and reduced viscosity (fig. S21).

We further investigated the printing resolutions of DAVP by continuously scanning a line under different printing settings. An expanding heated region instantly formed at the front of the scanning FUS focus, as a result of the thermal diffusion within the ink, which was also confirmed by sonothermal modeling (Fig. 2D, fig. S22, table S4, and movie S7). The sono-ink was cross-linked only at the center of the heating zone, where the temperature increased above the curing threshold, forming anisotropic filaments. We also investigated the dependence of the curing size on several key parameters, including the scanning speed of the FUS focus, the FUS frequency and power, and thermal diffusion (figs. S23 to S25 and movie S8). Modeling results showed that the thin ink tank (6 mm) caused heat accumulation at the tank boundary, whereas a thicker tank (>10 mm) allowed for normal thermal

diffusion around the focal region (fig. S26). Therefore, we used the 10-mm-thick ink tank to quantify the curing sizes (or printing resolutions) (Fig. 2E). First, increasing the scanning speed can improve the printing resolution. We observed overcuring in the longitudinal dimension (larger than design) at a slow scanning speed with all three ultrasound frequencies (2.05, 3.41, and 6.86 MHz), owing to excess heat accumulation. In comparison, undercuring (lower than design) was observed at high scanning speeds because of inadequate temperature increase at the two ends. The in-plane curing size was determined by the joint effect of the FUS scanning speed and thermal diffusion. For instance, the in-plane curing size at 3.41 MHz was improved from 7.6 mm to 1.6 mm by increasing the scanning speed from  $0.4 \text{ mm s}^{-1}$  to  $0.8 \text{ mm s}^{-1}$ . Similarly, the axial curing size was mostly determined by the FUS depth of focus and thermal diffusion. As an example, the 6.86-MHz FUS had a smaller depth of focus (1.69 mm) than the 2.05-MHz FUS (5.58 mm), but the sono-ink had a 10-fold acoustic absorption at 6.86 MHz and thus much higher heating efficiency. Eventually, the axial curing size ranged from 5.0 to 9.9 mm for the investigated printing parameters. The depth of focus here is defined as the size of the focal zone along the acoustic axis, in which the acoustic pressure drops to half of the peak value (table S5).

The printing resolution of DAVP can be flexibly adjusted by optimizing the FUS scanning speed, frequency, and power. Generally, the printing anisotropy (ratio of the axial and in-plane curing size) increased with the printing speed, mostly as a result of the decreased in-plane curing size (Fig. 2F). For example, when printing at  $0.8 \text{ mm s}^{-1}$  by the 6.86-MHz FUS, the cross section of printed filaments exhibited an oval shape with an axial size of 8.8 mm, which was 100% larger than the in-plane curing size (Fig. 2, G and H). The sonothermal curing mechanism also led to different microstructures within the FUS heating zone. The cured hydrogels displayed sub-micrometer pores in the PEGDA/PNIPAm matrix due to polymerization-induced phase separation, as shown by scanning electron microscopy (SEM) (Fig. 2I). SEM images suggested melting of agar microparticles owing to a high temperature of  $>85^\circ\text{C}$  at the center of the heating zone (Fig. 2I, panel ii). However, the agar microparticles maintained a granular shape outside the center of the focal zone at various printing speeds and frequencies, similar to that achieved by bulk heating at  $60^\circ$  to  $70^\circ\text{C}$  (figs. S28 and S29). These results further excluded the presence of FUS-induced cavitation and confirmed the heat accumulation-based curing mechanism. Meanwhile, the enhanced surface quality of the printed filaments was confirmed by the uniform and smooth surface (fig. S29D).



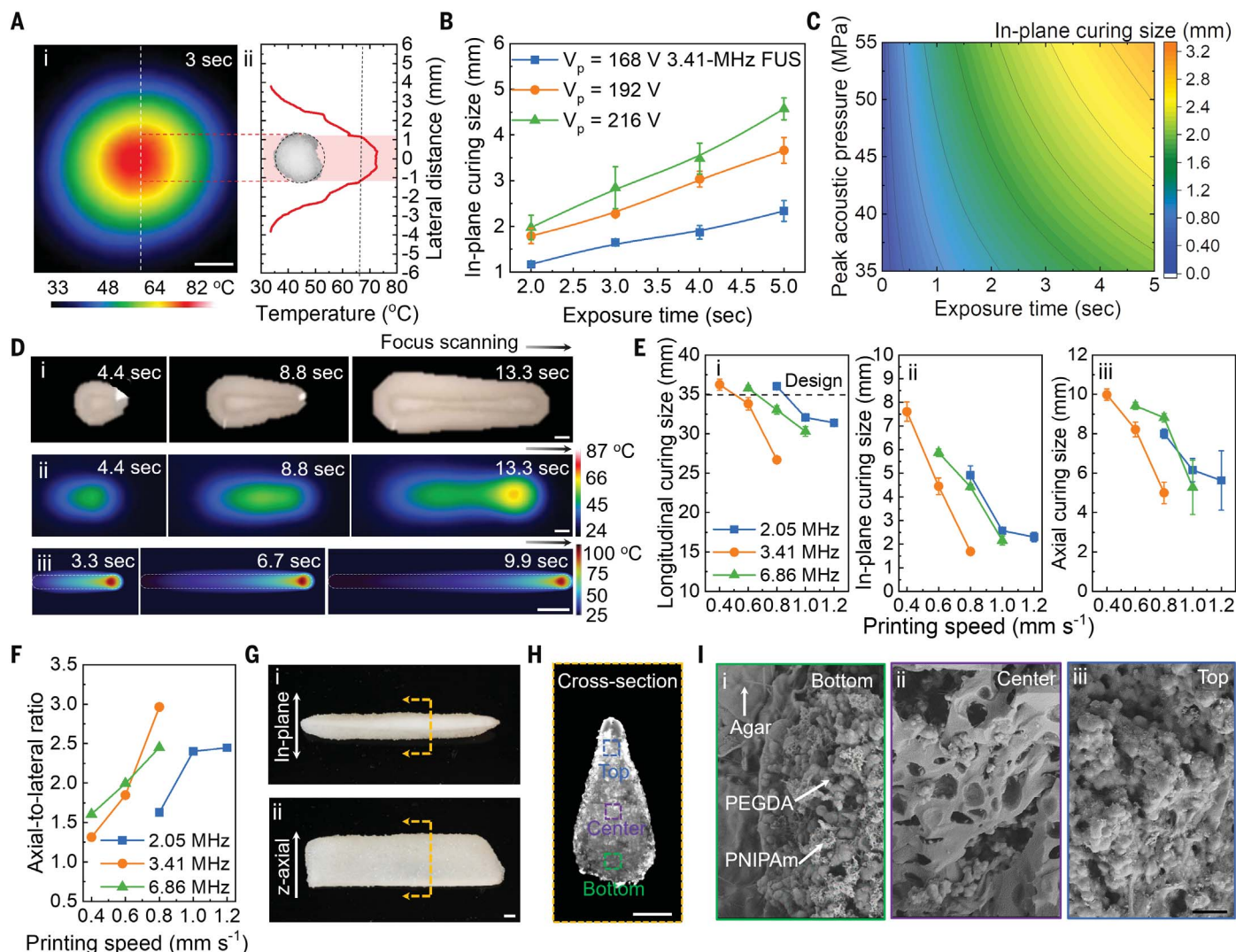


**Fig. 2. Characterizations of DAVP printing resolution.** (A) Typical surface temperature profile near the FUS focal region. The IR thermal image shows the in-plane temperature map (i) and temperature diagram at the cross section (ii). The inset shows the cured solid after 3-s FUS exposure (3.41 MHz) with the curing threshold temperature of 67°C. (B) In-plane curing size of printed solids versus FUS exposure time using PEGDA-based sono-ink (0.5 w/w% APS) at different  $V_p$ , as labeled. (C) Color-contour of modeled in-plane curing size at 3.41 MHz as a function of acoustic pressure and exposure time. (D) Snapshots of photographs (i) and IR thermal images (ii) near the FUS focal zone, as well as modeled temperature map on the focal plane (iii) at different time points during

line printing using PEGDA-based sono-ink (1.0 w/w% APS) (FUS frequency: 3.41 MHz; printing speed: 1.5 mm s<sup>-1</sup>). (E) Curing sizes for single-line DAVP printing using different printing speeds at various FUS frequencies as labeled: longitudinal size (i), in-plane size (ii), and z-axis size (iii). (F) Axial-to-lateral curing size ratio as a function of printing speed using various FUS frequencies, as labeled. (G) Photographs of printed filaments by single-line DAVP (6.86-MHz FUS) at a speed of 0.8 mm s<sup>-1</sup>: in-plane size (i) and axial size (ii). (H) Cross-sectional micrographs of printed filaments in (G) with three different marked regions. (I) SEM images of dried hydrogels in (H) at different regions: top (i), center (ii), and bottom (iii). Scale bars: 2 mm [(A), (D), (G), (H)] and 2 μm (I).

When performing multipath printing, the axial printing size (or printing thickness) increased, as a result of repeated FUS exposure along the acoustic axis at the scanned regions; however, the printing lengths were less sensitive to the number of printing paths (fig. S30). Additionally, the printing performance of DAVP was independent of the line-scanning direction of the 3D FUS printer. There were no significant differences in printing fidelity and mechanical properties (e.g., Young's moduli:  $1.4 \pm 0.1$ ,  $1.2 \pm 0.3$ , and  $1.3 \pm 0.1$  MPa) using different scanning directions (0°, 45°, and 90°,

respectively) (fig. S31). Moreover, the printed sample at the 0° infill angle showed significantly higher stiffness than that by bulk heating ( $0.9 \pm 0.1$  MPa), likely because of the high temperature-induced fast matrix curing and agar welding.

#### DAVP of volumetric constructs and material generality

Deep penetration is the primary advantage of DAVP over conventional light-based 3D printing (Fig. 3A). For example, in a black-dyed sono-ink (0.5 w/w%), the penetration depths

for the 2.05-, 3.41-, and 6.86-MHz ultrasound waves were 295.2, 86.8, and 28.2 mm at room temperature, respectively, which were, respectively, 600, 180, and 60 times as large as those for the 405-nm light ( $D_p = 0.48$  mm) (Fig. 3B). As such, a large curing depth of 24 mm in the dyed sono-ink was achieved in 26 s at an axial scanning speed of 1 mm s<sup>-1</sup> and 3.41-MHz FUS, whereas only a thin solid (2.4 mm) in the dye-stained photoink was obtained after photocuring for 165 s (fig. S32). The large penetration depth of DAVP, regardless of the optical properties of the ink, allowed us to volumetrically

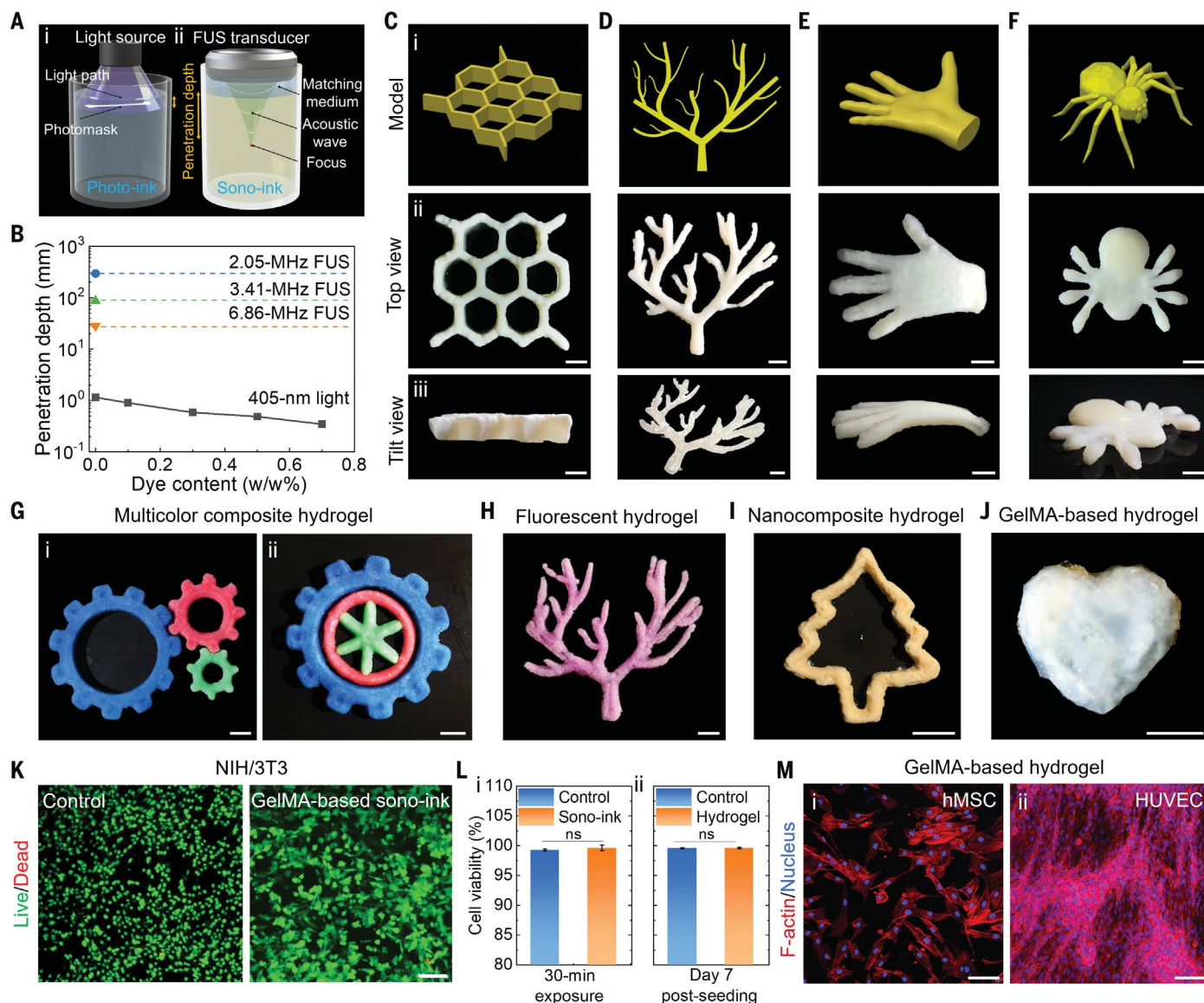


**Fig. 3. DAVP performance and material generality.** (A) Schematic illustrations for photocuring of photoinks (i) and FUS-curing of sono-inks (ii) with different penetration capabilities. (B) Penetration depth as a function of black-dye content for UV light (405 nm) and FUS at different frequencies, as labeled. (C to F) Design models (i), top-view (ii), and tilt-view photographs (iii) of printed constructs of various shapes using PEGDA-based sono-ink: honeycomb (C), vessel network (D), 3D hand (E), and spider (F). (G to J) Photographs of printed constructs using various sono-inks: multicolor three-part gear set (i) and a three-part wheel set (ii) by dye-stained PEGDA-based sono-inks consisting of different colors (G), vascular network model by a fluorescence-stained PEGDA-based sono-ink (0.1 w/w% rhodamine B) (H), tree-shaped model by a PEGDA-based nanocomposite sono-ink

(10 wt % nanoclay) (I), and layered heart-shaped model by a GelMA-based protein sono-ink (J). (K to M) In vitro cytocompatibility of GelMA-based sono-inks and cured hydrogels: representative fluorescence micrographs of live (green)/dead (red) cells (NIH/3T3 fibroblasts) after 30-min exposure to DPBS (control) and GelMA-based sono-ink (K), quantitative cellular viability values of NIH/3T3 fibroblasts after 30-min exposure to GelMA-based sono-ink (i) and at day 7 after seeding on GelMA-based hydrogel (ii) (L), fluorescence micrographs showing F-actin staining of cells at day 7 after seeding on the GelMA/PNIPAm hydrogel using two cell types: human mesenchymal stem cells (hMSCs) (i) and human umbilical vein endothelial cells (HUVECs) (ii). F-actin, red; nucleus, blue. ns, no significant difference. Scale bars: 10 mm [(C) to (J)] and 100  $\mu$ m [(K) and (M)].

print nontransparent 2D and 3D hydrogel constructs with different sizes and geometrical complexities, including letters and lattices with sharp corners and spirals and vessels with smooth surfaces and transitions (fig. S33, table S6, and movie S9). For example, a 10-layer honeycomb and a vascular network were printed at 3.41 MHz (Fig. 3, C and D, and table

S6). A complex 3D hand model (67 mm by 53 mm by 10 mm) and a spider model (52 mm by 43 mm by 10 mm) were also printed at 6.86 MHz (Fig. 3, E and F; fig. S34; and table S6).

Using dye-stained PEGDA-based sono-inks, we printed opaque-colored hydrogel composites for prototypes, including a set of three gears of different sizes and an assembled wheel

set of three colored parts (Fig. 3G and fig. S35). Altering the phase-transition polymers with higher  $T_t$ , such as poly(*N*-isopropylmethacrylamide) (PNIPMAM), could facilitate printing at body temperature (37°C) (fig. S35D). Additionally, fluorescence-stained sono-ink (0.1 wt % rhodamine B) was used to print a high-fidelity branched vascular network shape (81 mm by



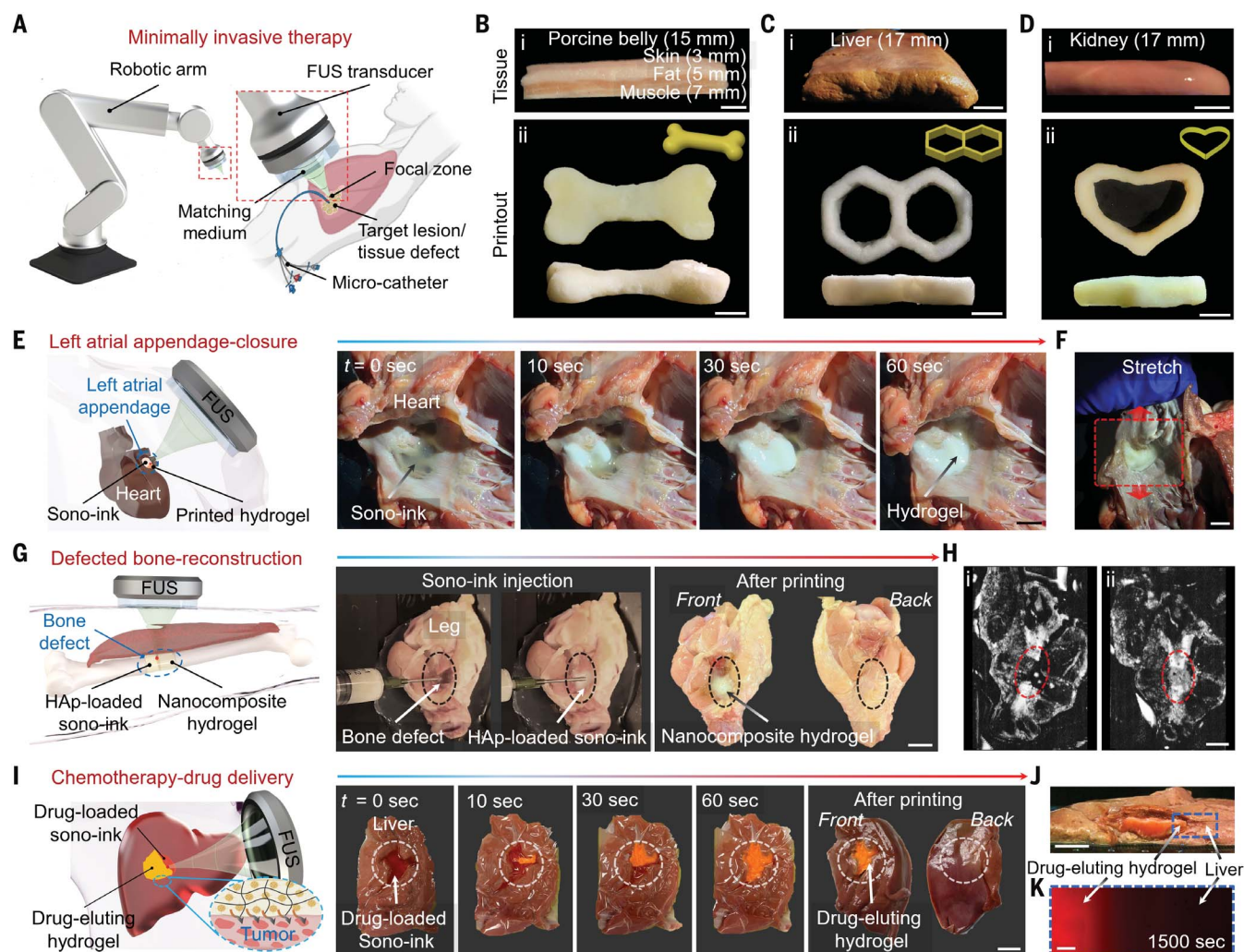


**Fig. 4. DAVP for proof-of-concept through-tissue printing and minimally invasive therapy.** (A) Scheme of minimally invasive therapy by through-tissue manufacturing of scaffolds on target lesions and tissues. (B to D) Tissue phantoms with marked thicknesses (i) and printed objects with associated digital models (ii) for through-tissue manufacturing: a bone-shaped model printed under porcine belly (B), a lattice printed under porcine liver (C), and a heart-shaped model printed under porcine kidney (D). Printing was performed with 2.05-MHz FUS at  $0.6 \text{ mm s}^{-1}$ . (E and F) DAVP for LAA closure for a 12-mm-thick goat heart: scheme and printing process at different time points (E), and stretching of closed LAA (F). (G and H) DAVP for

defective bone reconstruction: scheme and photographs showing the procedures of manufacturing a nanocomposite filler material on a bone defect through 10-mm-thick skin and muscle (G), and ultrasound images of the bone defect (i) and the reconstructed bone (ii) (H). (I to K) DAVP for chemotherapy drug delivery for a 14-mm-thick porcine liver: scheme and photographs showing the procedure of printing drug-eluting hydrogels using a doxorubicin-loaded sono-ink on a liver lesion (I), cross-sectional photograph showing the printed hydrogel-liver interface (J), and fluorescence micrograph showing drug diffusion from the printed drug-eluting filler hydrogel to the liver at 1500-s contact (K). Scale bars: 10 mm [(B) to (J)] and 200  $\mu\text{m}$  (K).

70 mm by 3 mm) (Fig. 3H). Further, a nanocomposite sono-ink consisting of 10 wt % nanoclay was exploited to print a four-layer tree shape (2 mm in thickness) (Fig. 3I). DAVP was also used to print protein-based biomaterials, as suggested by the tough-hydrogel heart model using the GelMA-based sono-ink (Fig. 3J and fig. S35, E and F). Both PEGDA- and GelMA-based sono-inks and their key components exhibited zero to low cytotoxicity using NIH/3T3 fibroblasts as a model cell line. High cell viability (>99%) similar to the control [using Dulbecco's phosphate-buffered saline (DPBS)] was observed after direct and indirect exposure to the sono-ink for up to 30 min (Fig. 3, K

and L, and fig. S36). Moreover, similar to the control cultured in a petri dish, the GelMA-based hydrogel enabled high viability (>99%) and healthy attachment and proliferation of postseeded mammalian cells of different types (Fig. 3M and fig. S37), indicating its favorable bioactivity.

#### DAVP for through-tissue printing and constructive minimally invasive medicine

As a proof of concept, we applied DAVP for high-speed and high-resolution through-tissue manufacturing and minimally invasive medicine (Fig. 4A). First, we illustrated the ex vivo through-tissue printing using soft tissues of

different types and dimensions (fig. S38 and table S7). For through-tissue printing, thick tissues (up to 17 mm thick) were placed on top of the sono-ink chamber in the FUS near field. We printed a bone-shaped construct at 2.05 MHz through an ex vivo porcine tissue phantom consisting of a skin layer (3 mm), a fat layer (5 mm), and a muscle layer (7 mm) (Fig. 4B). High-fidelity honeycombs were printed through a 15-mm-thick porcine tissue consisting of skin and muscle or a 17-mm-thick porcine liver tissue (Fig. 4C). Similarly, a hollow heart-shaped model was printed through a 17-mm-thick porcine kidney tissue (Fig. 4D and movie S10).

Nonvalvular atrial fibrillation is a prevalent cardiovascular disease related to the left atrial appendage (LAA) (41, 42). Open-chest surgery or transcatheter procedures can seal off the LAA to reduce the risk of thromboembolism. However, surgical LAA closure is severely invasive, and the treatment is often incomplete (41). We demonstrated proof-of-concept DAVP-assisted LAA closure (Fig. 4E). We delivered the sono-ink through a catheter to the LAA of an ex vivo goat heart placed in the printing chamber. The sono-ink was then solidified using the 3D FUS printer at 3.41 MHz through a 12-mm-thick heart wall. Precise FUS focus scanning enabled selective curing of the sono-ink within the entire LAA volume while sparing surrounding heart tissues (fig. S39 and movie S11). After treatment, the cured hydrogels completely occluded the LAA and bonded well with the tissue wall, which could tolerate reasonable distortions that mimicked the heart beating (Fig. 4F).

We further explored the potential of the DAVP technique for tissue reconstruction and regeneration, such as treating large bone defects (43). As an illustration, the PEGDA/agar/PNIPMAm nanocomposite sono-ink consisting of 5 w/w% hydroxyapatite (HAp) nanoparticles was formulated to print a bone scaffold for a hypothetical bone loss treatment (Fig. 4G and movie S12). We used a chicken leg to create a fibula bone defect model (1 cm long). After injecting the nanocomposite sono-ink, we printed a beam-shaped HAp-laden composite material through the skin and muscle tissues (10 mm thick) to reshape the defective volume. The nanocomposite material could reconstruct the bone with seamless bonding to the native parts without influencing the surrounding tissues, as confirmed by ultrasound imaging (Fig. 4H).

We also demonstrated DAVP for therapeutic drug delivery by printing drug-eluting filler hydrogels on liver lesions (Fig. 4I). Doxorubicin, a clinical chemotherapy drug for treating a wide range of cancers, such as breast cancer and hepatocellular carcinoma, was used as a model drug (44). PEGDA/agar/PNIPMAm sono-ink consisting of 1 mg ml<sup>-1</sup> of doxorubicin was formulated for printing chemotherapy drug-eluting hydrogels at the liver lesion sites at 37°C using FUS at various frequencies (fig. S40). DAVP enabled through-tissue printing and selective curing, as shown by the intimate hydrogel-tissue interfacial bonding (front side) and negligible burning of the intervening tissue (back side) (Fig. 4J and movie S13). The drug in the hydrogel gradually released and diffused into the liver tissue (effective diffusivity:  $8.7 \times 10^8$  cm<sup>2</sup> s<sup>-1</sup>), forming an ~3-mm-thick effective therapeutic layer [5.8 µg ml<sup>-1</sup> concentration (44)] within 7 days by modeling (Fig. 4K and fig. S41). We anticipated that this method could be used as postablative chemotherapy to improve cancer treatment.

We note that relatively high FUS energies were needed for through-tissue printing, mainly because of the acoustic attenuation by the intervening tissues. The acoustic energy loss might possibly result in overheating of the intervening tissues. To mitigate the risk of tissue overheating and to improve future in vivo printing efficiency, we developed a confocal-DAVP system in which the 3D FUS printer used two FUS transducers aligned in a cross-beam pattern, with their acoustic axes 90° apart and their foci overlapping (fig. S42). Taking advantage of the energy superposition of two acoustic foci, confocal-DAVP can achieve the curing temperature threshold in the combined foci, using roughly half of the output energy from each FUS transducer. Such a confocal configuration has two advantages: (i) the acoustic energy deposition in the local intervening position is reduced by ~50%, and thus the overheating risk is minimized; (ii) the printing resolution and speed can be improved, owing to better sonothermal confinement within the overlapped foci. Indeed, the axial printing resolution was improved to 0.7 mm, and the printing speed reached 8 mm s<sup>-1</sup> (fig. S42). Accordingly, complex models, including a leaf-shaped structure (55 mm by 35 mm) and a vessel-like network (75 mm by 25 mm), were successfully printed using the confocal-DAVP, taking only 20 and 83 s, respectively (fig. S43, table S8, and movie S14).

## Conclusions

Leveraging the deep-penetration capability of FUS waves, low acoustic streaming, and rapid sonopolymerization of the viscoelastic self-enhancing sono-inks, we have developed a DAVP technique that can volumetrically build constructs with high printing fidelity and resolution in the absence of a build platform. The use of a thermally responsive adaptive acoustic absorber resolves the conflict between acoustic streaming and deep penetration upon FUS exposure. The self-enhancing sono-ink and nonlinear acoustic propagation collectively enhanced the sonothermal heating at the FUS focus for fast and selective material solidification as the building voxel. The heat accumulation-based curing mechanism resulted in anisotropic printing resolution at a millimeter scale, which may be further improved by optimizing printing parameters of FUS frequency and scanning speed and by using the confocal dual-transducer configuration. The deep penetration of FUS waves allows the volumetric fabrication of opaque (nano)composites and printing through centimeter-thick tissues that are not attainable through state-of-the-art light-based printing techniques (table S9). The self-enhancing sono-ink design can be generalized for different systems, greatly expanding the materials library for acoustic printing techniques.

## REFERENCES AND NOTES

- J. R. Tumbleston et al., *Science* **347**, 1349–1352 (2015).
- S. Gantenbein et al., *Nature* **561**, 226–230 (2018).
- X. Zheng et al., *Science* **344**, 1373–1377 (2014).
- M. A. Skylar-Scott, J. Mueller, C. W. Visser, J. A. Lewis, *Nature* **575**, 330–335 (2019).
- K. Liu, R. Sun, C. Daraio, *Science* **377**, 975–981 (2022).
- H. Wei et al., *Nat. Commun.* **12**, 2082 (2021).
- H. Yuk et al., *Nat. Commun.* **11**, 1604 (2020).
- Y. Y. C. Choong et al., *Nat. Rev. Mater.* **5**, 637–639 (2020).
- L. Moroni et al., *Nat. Rev. Mater.* **3**, 21–37 (2018).
- A. Lee et al., *Science* **365**, 482–487 (2019).
- S. C. Ligon, R. Liska, J. Stampfl, M. Gurr, R. Mülhaupt, *Chem. Rev.* **117**, 10212–10290 (2017).
- M. L. Bedell, A. M. Navara, Y. Du, S. Zhang, A. G. Mikos, *Chem. Rev.* **120**, 10744–10792 (2020).
- D. A. Walker, J. L. Hedrick, C. A. Mirkin, *Science* **366**, 360–364 (2019).
- M. P. de Beer et al., *Sci. Adv.* **5**, eaau8723 (2019).
- S.-F. Liu et al., *Science* **377**, 1112–1116 (2022).
- F. Han et al., *Science* **378**, 1325–1331 (2022).
- N. M. Larson et al., *Nature* **613**, 682–688 (2023).
- G. Villar, A. D. Graham, H. Bayley, *Science* **340**, 48–52 (2013).
- X. Kuang et al., *Sci. Adv.* **5**, eaav5790 (2019).
- M. Shusteff et al., *Sci. Adv.* **3**, eaao5496 (2017).
- P. N. Bernal et al., *Adv. Mater.* **31**, e1904209 (2019).
- B. E. Kelly et al., *Science* **363**, 1075–1079 (2019).
- M. Xie et al., *Nat. Commun.* **14**, 210 (2023).
- M. Regheby et al., *Nature* **588**, 620–624 (2020).
- D. Loterie, P. Delrot, C. Moser, *Nat. Commun.* **11**, 852 (2020).
- S. N. Sanders et al., *Nature* **604**, 474–478 (2022).
- J. Wong et al., *Adv. Mater.* **35**, e2207673 (2023).
- J. Zhu, Q. Zhang, T. Yang, Y. Liu, R. Liu, *Nat. Commun.* **11**, 3462 (2020).
- M. Lee, R. Rizzo, F. Surman, M. Zenobi-Wong, *Chem. Rev.* **120**, 10950–11027 (2020).
- Y. Chen et al., *Sci. Adv.* **6**, eaba7406 (2020).
- T. G. McKenzie, F. Karimi, M. Ashokkumar, G. G. Qiao, *Chemistry* **25**, 5372–5388 (2019).
- B. Rokita, J. M. Rosiak, P. Ulanski, *Macromolecules* **42**, 3269–3274 (2009).
- Z. Gao et al., *ACS Macro Lett.* **8**, 1285–1290 (2019).
- M. Habibi, S. Foroughi, V. Karamzadeh, M. Packirisamy, *Nat. Commun.* **13**, 1800 (2022).
- R. T. Beyer, *Phys. Acoust.* **2**, 231–264 (1965).
- L. Claes et al., *Measurement* **184**, 109919 (2021).
- P. V. Yuldashev et al., *IEEE Trans. Ultrason. Ferroelectr. Freq. Control* **68**, 2837–2852 (2021).
- A. Rahimzadeh, M. Rutsch, M. Kupnik, R. V. Klitzing, *Langmuir* **37**, 5854–5863 (2021).
- A. Bhargava, V. C. Meesala, M. R. Hajji, S. Shahab, *Appl. Phys. Lett.* **117**, 064101 (2020).
- S. Haddadi, M. T. Ahmadian, *Sci. Iran.* **25**, 2087–2097 (2018).
- D. R. Holmes Jr., T. J. Simard, A. M. Killu, M. A. Alkhoul, *Mayo Clin. Proc.* **97**, 1525–1533 (2022).
- H. Ueno, T. Imamura, S. Tanaka, N. Fukuda, K. Kinugawa, *J. Cardiol.* **81**, 420–428 (2023).
- A. Stahl, Y. P. Yang, *Tissue Eng. Part B Rev.* **27**, 539–547 (2021).
- L. Barraud et al., *J. Hepatol.* **42**, 736–743 (2005).
- X. Kuang et al., Self-enhancing sono-inks enable deep-penetrating acoustic volumetric printing, *Zenodo* (2023); <https://doi.org/10.5281/zenodo.8422050>.

## ACKNOWLEDGMENTS

This work was performed in part at the Center for Nanoscale Systems (CNS) at Harvard University, a member of the National Nanotechnology Infrastructure Network (NNIN), which is supported by the National Science Foundation under award number ECS0335765. We also thank D. A. Weitz from Harvard University for rheometer access, and P. Zhong from the Department of Mechanical Engineering and Materials Science at Duke University for assistance with acoustic cavitation mapping. **Funding:** This work is supported by the National Institutes of Health (R21EB025270, R01HL153857, R01HL165176, R01HL166522, and R01CA282451), the National Science Foundation (CBET-EBMS-1936105), and the Brigham Research Institute, all to Y.S.Z.; National Institutes of Health (NIH) [R21EB027981, R21EB027304, RF1NS115581 (BRAIN Initiative), R01NS111039, R01EB028143, R21EB027981, and R01EB031629], National Science Foundation

CAREER award 2144788, and Chan Zuckerberg Initiative Grant 2020-226178, all to J.Y. M.O.A. acknowledges funding support from the TÜBİTAK 2214-A Program (1059B141801395). **Author contributions:** X.K., J.Y., and Y.S.Z. conceived of the idea. X.K. designed the materials and methods. Q.R., S.B., X.K., M.C., T.V., and C.E.G.-M. designed the printer setup. X.K., A.M.L.L., and M.O.A. prepared the materials and conducted material characterizations. Q.R., S.B., T.V., N.W., and X.K. performed the printing and acoustic characterizations. Q.R. and X.K. developed the numerical models and conducted the simulations. X.K., Q.R., S.B., T.V., N.W., and C.E.G.-M. analyzed the results and processed visualizations. X.K., J.Y., and Y.S.Z. wrote the manuscript, with input

from all authors. Y.S.Z. and J.Y. supervised the study. **Competing interests:** Y.S.Z. consults for Allevi by 3D Systems and sits on the scientific advisory board and holds options of Xellar, neither of which, however, participated in or biased this work. **Data and materials availability:** All data needed to evaluate the conclusions in the study are present in the paper and/or the supplementary materials. G-codes for printing and simulation codes for diffusion analysis are provided on Zenodo (45). **License information:** Copyright © 2023 the authors, some rights reserved; exclusive licensee American Association for the Advancement of Science. No claim to original US government works. <https://www.science.org/about/science-licenses-journal-article-reuse>

#### SUPPLEMENTARY MATERIALS

[science.org/doi/10.1126/science.adl1563](https://science.org/doi/10.1126/science.adl1563)  
Materials and Methods  
Supplementary Text  
Figs. S1 to S43  
Tables S1 to S9  
References (46–81)  
MDAR Reproducibility Checklist  
Movies S1 to S14

Submitted 6 April 2023; accepted 13 October 2023  
10.1126/science.adl1563